AGU PUBLICATIONS

Earth and Space Science

RESEARCH ARTICLE
10.1002/2015EA000116

Observations of the ionospheric impact of M-class solar flares on local and hemispheric scales

J. F. Helmboldt[1], N. E. Kassim[1], and S. W. Teare[2]

[1]U.S. Naval Research Laboratory, Washington, District of Columbia, USA, [2]Department of Electrical Engineering, New Mexico Tech, Socorro, New Mexico, USA

Key Points:
- Even moderate-strength solar flares cause large-scale ionospheric disturbances
- The most noticeable feature is a hemispheric, step-like increase in TEC
- More subtle ionospheric and plasmaspheric disturbances were also observed on smaller scales

Supporting Information:
- Movie S1 caption
- Movie S1

Correspondence to:
J. F. Helmboldt,
Joe.Helmboldt@nrl.navy.mil

Citation:
Helmboldt, J. F., N. E. Kassim, and S. W. Teare (2015), Observations of the ionospheric impact of M-class solar flares on local and hemispheric scales, *Earth and Space Science*, *2*, doi:10.1002/2015EA000116.

Received 17 MAY 2015
Accepted 7 SEP 2015
Accepted article online 18 SEP 2015

Abstract The ionospheric impact of a series of M-class solar flares that occurred on 12 March 2015 is described. A combination of data sets from GPS receivers and two different colocated radio telescopes, the very large array (VLA) and the long wavelength array (LWA), was used to detect and characterize flare-induced irregularities. The data demonstrate that each flare causes a rapid step-like increase in total electron content (TEC) of about 0.2 total electron content units (TECU), 1 TECU = 1016 el m^{-2}. The rise times of these steps are on the order of 1–3 min. The GPS data show signs of traveling ionospheric disturbances likely associated with gravity waves whose magnitudes were temporarily enhanced by the impact of two of the flares. Increased activity within the horizontal TEC gradients observed with the VLA was apparent for several minutes following the flare X-ray peak. The properties of these VLA-detected disturbances are strongly indicative of field-aligned irregularities within the plasmasphere. They initially form at two altitudes, approximately 2600 and 5600 km. Those that form higher quickly disappear, whereas those that form lower appear to descend over a period of ~7 min to an altitude of roughly 1450 km before disappearing. LWA observations of ionospheric reflections of the HF radio station WWV show a significant and brief (~few minutes) Doppler frequency disturbance near the onset of TEC enhancement, followed by a ~5 min drop in received power, indicating increased ionization in the *D* region.

1. Introduction

High-energy photons from the Sun are chiefly responsible for the ionization of portions of Earth's thermosphere during the day, leading to the region commonly referred to as the ionosphere. Thus, any change in the output of these photons has a direct impact on the state of the ionosphere. While gradual changes within a solar cycle lead to large-scale spatial and temporal variations in ion and electron density within the ionosphere, brief events like solar flares have a more abrupt and relatively extreme effect.

Decades of observations and simulations have established solar flares as the cause of so-called sudden ionospheric disturbances (SIDs). Perhaps the most well-known manifestation of an SID is a sudden phase advance observed within systems monitoring long-distance VLF propagation [*Field*, 1970; *Matsushita*, 1976; *Vazherkin et al.*, 1980; *Kaufmann et al.*, 2002; *Pacini and Raulin*, 2006]. Another classic feature of a flare-induced SID is a sudden, minute-long reduction in received power for HF systems due to increased ionization and subsequent absorption within the *D* region [*Ellison*, 1950; *Appleton and Piggott*, 1954; *Atac*, 1991]. Flares have also been observed to have a measurable effect on the total election content (TEC) determined with GPS receivers [*Afraimovich et al.*, 2000; *Liu et al.*, 2004; *Tsugawa et al.*, 2007a; *Leonovich and Tashchilin*, 2008]. Flare-associated disruptions also coincide with notable variations within the geomagnetic field (e.g., "crochets") [*Dodson and Hedeman*, 1958; *Dmitriev and Yeh*, 2008; *Qian et al.*, 2012]. Not surprisingly, the ionospheric impact of flares is related to some degree with the strength of the flares [e.g., *Kaufmann et al.*, 2002]. In fact, GPS-based observations of the ionospheric impacts of flares have been and are being used as proxies for measurements of the flares' EUV photon flux rates [*Hernández-Pajares et al.*, 2012a].

This paper focuses on the analysis of observations of the relatively subtle ionospheric impact of a series of four moderate (class M) solar flares that occurred on 12 March 2015. We use a combination of GPS data and observations made serendipitously with two radio frequency (RF) telescopes in central/western New Mexico. The GPS data show small but significant increases in TEC on hemispheric scales associated with all four flares. Smaller-scale ionospheric and plasmaspheric fluctuations were found and characterized with the RF telescopes during the final flare, the only one during which they were observing. The data collections and

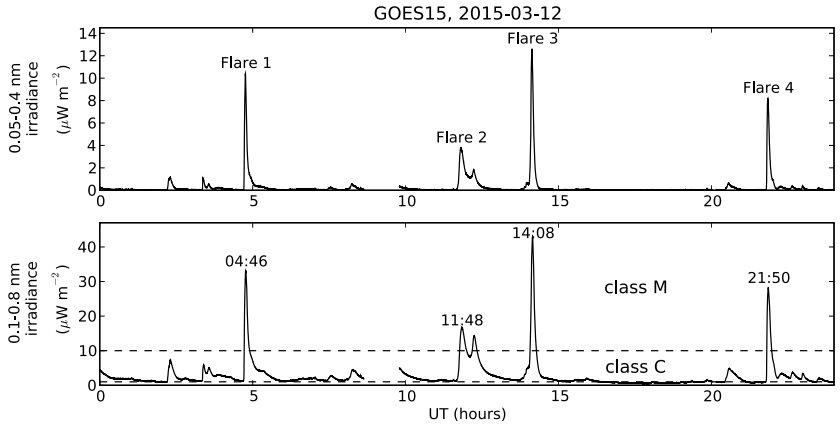

Figure 1. X-ray irradiance time series from the GOES15 satellite for 12 March 2015. (top) The four M-class flares are labeled. (bottom) The peak times of the flares are printed above each, and the boundaries for the X-ray classes M and C are shown with dashed lines.

instruments used are described and the analysis presented in section 2. The results are discussed further in section 3.

2. Data Collection and Analysis

In the runup to the G4-class geomagnetic storm of 17 March 2015, there were many solar flares of varying magnitudes. As stated above, this paper focuses on those occurring on 12 March due to the serendipitous collection of data during one flare from two RF telescopes that are particularly sensitive to small-scale ionospheric (and sometimes plasmaspheric) fluctuations. There were, however, several flares that day, as one can see from the X-ray irradiance measured by the GOES15 satellite plotted in Figure 1. The GOES15 data show four M-class flares as well as four to six smaller class C flares. For convenience, we will refer to the M-class events as Flares 1–4, and they are labeled as such within Figure 1 (top). The peak time (UT) for each of these is also printed within Figure 1 (bottom).

For each M-class flare, we also obtained and examined the GOES15 Solar X-ray Imager images near in time to the flare. We found that all four occurred within the Southern Hemisphere within about 0.2–0.3 solar radii of the observed center of the solar disk. The exact distances from the center measured from these images are given in Table 1 as r/R_S along with the peak times (UT) and irradiances within both X-ray bands.

2.1. GPS Data and Hemispheric Impact

GPS receivers have become a powerful tool for ionospheric remote sensing over the past few decades. The relatively dense coverage of continuously operating GPS receivers within many parts of the world allows for the generation of detailed maps of TEC derived from the differential ionospheric delay imposed on the two GPS frequencies ($L1 = 1575.42$ MHz; $L2 = 1227.60$ MHz).

To examine the large-scale effects of the 12 March solar flares on the ionosphere, we first obtained GPS-derived absolute, vertical TEC data from Massachusetts Institute of Technology (MIT) Haystack Observatory Madrigal database. These data are generated at 5 min intervals using all available GPS data with corrections for viewing angle and instrumental bias applied. We binned these data by time and longitude for the continental United States (CONUS) and show the mean TEC within these bins as an image in Figure 2 (top). From this,

Table 1. Flare X-ray Properties

Flare No.	Peak UT	I_{max}(0.05–0.4 nm) (μW m^{-2})	I_{max}(0.1–0.8 nm) (μW m^{-2})	r/R_S
1	4.76	10.39	32.33	0.32
2	11.80	3.75	15.26	0.26
3	14.13	12.58	40.50	0.18
4	21.84	8.18	27.54	0.18

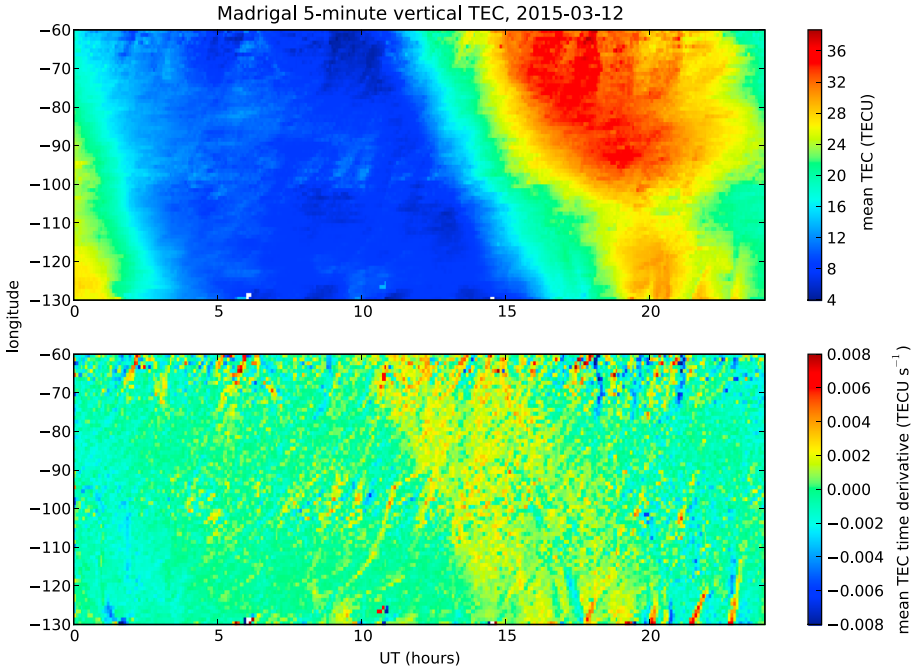

Figure 2. Images of the mean absolute vertical TEC from the MIT Madrigal database as functions of time and longitude for the continental United States (CONUS) at 5 min and 1° resolution. (top) TEC and (bottom) temporal derivative of TEC within each longitude bin.

one can clearly see the normal diurnal variation in TEC, with some longitudinal structure, but no sign of the impact of flares. To highlight fluctuations in TEC, we also computed the time derivative of the mean TEC for each longitude bin and show the resulting image in Figure 2 (bottom). While some disturbances and/or artifacts are evident, they do not appear to coincide with any of the X-ray-detected flares.

The typical uncertainty reported for the TEC values from the Madrigal database is 2–3 total electron content units (TECU), 1 TECU = 10^{16} el m^{-2}, implying that small-amplitude fluctuations will not be evident within these data. Given the 5 min temporal resolution, short-duration disturbances will also be difficult to visualize using these data. Therefore, to search for more subtle changes in TEC, we obtained data from 2058 continuously operating GPS receivers within CONUS from four different databases: the International Global Navigation Satellite Systems Service, the Continuously Operating Reference Stations, the University Navstar Consortium, and the Scripps Orbit and Permanent Array Center. The data were obtained in Receiver Independent Exchange (RINEX) format and processed with the GPS Toolkit (GPSTk) [*Munton et al.*, 2004] to extract relative slant TEC time series for each satellite/receiver pair. GPSTk was also used to compute the ionospheric pierce point (IPP) latitudes and longitudes assuming a height of 300 km. For all the analysis performed with these data, only instances where the satellite elevation was >30° were used to mitigate the effects of extreme viewing angles and cycle slips.

To remove the effect of instrumental bias and to highlight finer time scale TEC variations, the relative TEC time series were detrended using the finite differencing method described by *Hernández-Pajares et al.* [2006]. This technique allows one to specify a dominant time scale via a parameter, τ, such that the temporal frequency response for the resulting detrended data is $2\sin^2(\pi\tau f)$, where f is the temporal frequency (i.e., the reciprocal of the oscillation period). Thus, the response peaks at an oscillation period of 2τ. The relative TEC data were detrended with $\tau = 60$, 180, and 540 s, highlighting oscillation periods of 2, 6, and 18 min, respectively. The detrended CONUS data were then binned by UT and IPP longitude and averaged with temporal and longitudinal resolutions of 30 s and 0.1°. Images of these are shown for each value of τ for all of 12 March in Figure 3.

A close examination of the panels in Figure 3 (especially the high-resolution versions available electronically) shows clear signatures of the three M-class flares that were visible from North America (see the three regions highlighted with black boxes). They are especially apparent within the images for $\tau = 60$ and 180 s where

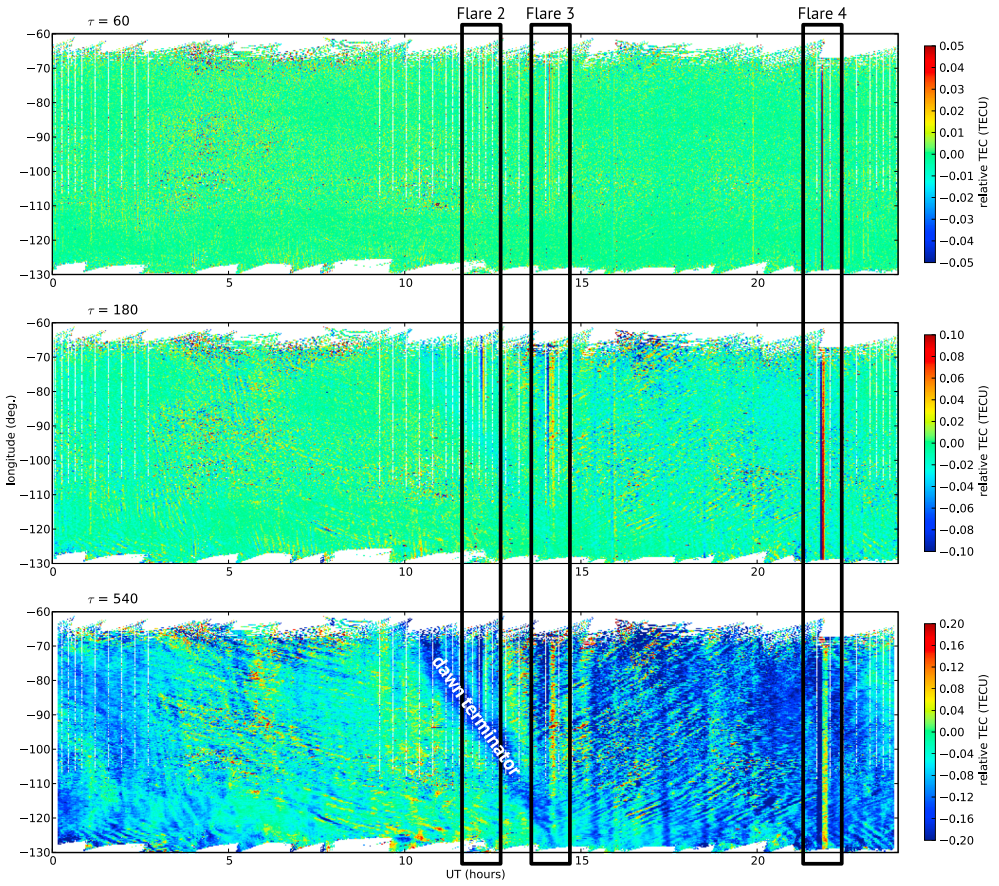

Figure 3. Images of mean relative TEC for CONUS with three different values of the detrending parameter τ (see section 2.1) at temporal and longitudinal resolutions of 30 s and 0.1°. The locations of the three M-class flares visible from CONUS (Flares 2–4) are highlighted with black rectangles in all panels; the depletion associated with the dawn terminator is labelled in Figure 3 (bottom).

other, longer-period disturbances evident within the $\tau = 540$ s image are dampened. For all three flares, the detrended relative TEC undergoes a kind of modulated pulse, resembling an inverted *N* wave. The initial TEC depletion and subsequent spike occur rather uniformly for all longitudes east of the dawn terminator. We note that we also examined the data for significant latitudinal variations and found evidence of none.

To verify that these signatures were present over an entire hemisphere and to access locations for which Flare 1 was visible, we also obtained RINEX data for all available receivers within continental Europe (EU). Within the publicly accessible databases used (see above), this region has by far the most complete coverage outside the CONUS region (145 receiver stations with data for 12 March). Still, the coverage was only good enough to make time/longitude images of relative TEC with 1° longitudinal resolution. These are displayed for each value of τ in Figure 4. Indeed, the EU data exhibit disturbances for the first three flares (Flare 4 was not observable from Europe) that have morphologies very similar to what is apparent within the images for the CONUS data. For the flares where both data sets have nearly complete longitudinal coverage during the pulses (Flares 2 and 3), the TEC magnitudes are roughly in agreement.

In Figures 5 and 6, we show 35 min sections of the images displayed in Figures 3 and 4 centered on the flare-induced TEC pulses. These "zoomed-in" images reveal much substructure within the individual pulses, especially within the higher-resolution CONUS data. The $\tau = 540$ s data appear more sensitive to these fluctuations, which by and large seem to be consistent with disturbances seen before and after the flares, just with different amplitudes (see the CONUS data for Flares 3 and 4 in particular). This suggests that the substructure within the pulses may simply be a reflection of irregularities present at the time of the flare that are decimated/enhanced by the TEC pulses. These appear to be largely consistent with typical traveling ionospheric disturbances (TIDs) with zonal speeds and wavelengths of ~100–150 m s^{-1} and ~1° (110 km),

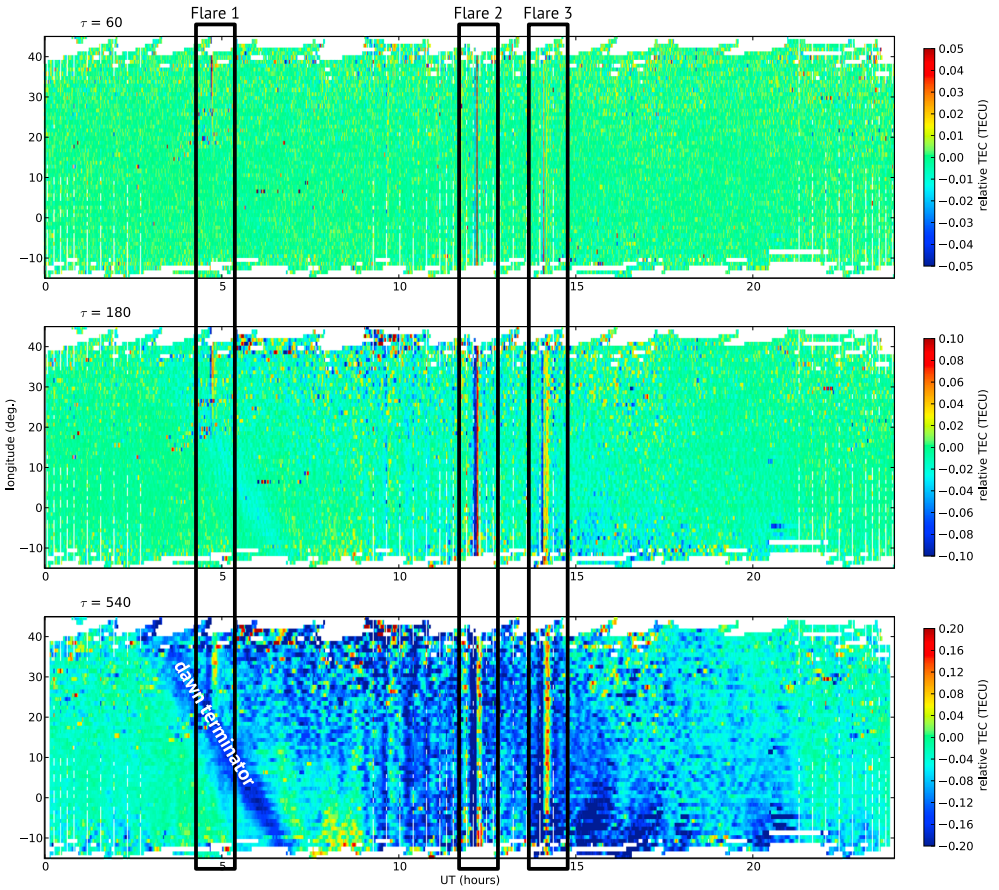

Figure 4. The same as Figure 3 but for Europe (EU). Here the temporal resolution is 30 s, and the resolution in longitude is 1°.

respectively [e.g., *Hernández-Pajares et al.*, 2006; *Tsugawa et al.*, 2007b; *Hernández-Pajares et al.*, 2012b]. During Flare 3, they are apparent mainly between the dawn terminator and 80°W; during Flare 4, they are confined to longitudes west of about 115°W.

The shapes of the TEC pulses for all flares and values of τ, namely, inverted *N* waves with roughly equal-magnitude minima and maxima, are what is expected to result from relatively simple step functions to which our chosen detrending method has been applied. For a rapid, step-like increase in TEC, the finite differencing method used will cause the time period before the step to appear depleted because the elevated TEC level has been (partially) subtracted from the baseline preflare TEC. Likewise, after the step increase, the detrended TEC time series appears elevated for a time period of $\simeq \tau$. For a relatively rapid step increase, the maxima and minima will together resemble a square wave; for slower rise times, the extrema will appear more rounded.

To highlight the overall morphologies of these step-induced pulses, we have plotted in Figure 7 the median TEC for each pulse and value of τ using all CONUS and EU data for IPPs east of the dawn terminator. For each time series, the median TEC within ±37.5 min of the flare peak was subtracted to remove any persistent, baseline value that survived the detrending process. To each of these, we have fit a detrended form of the following function

$$\mathrm{TEC}(t) = \begin{cases} \Delta\mathrm{TEC}\exp\left[\frac{-(t-t_{\mathrm{pk}})^2}{2t_r^2}\right], & \text{if } t < t_{\mathrm{pk}} \\ \Delta\mathrm{TEC}, & \text{if } t \geq t_{\mathrm{pk}} \end{cases} \quad (1)$$

where ΔTEC is the change in TEC due to the fare, t_{pk} is the time at which the TEC reaches its peak, and t_r parameterizes the rise time of the TEC step. The fits were performed using a standard Levenberg-Marquardt nonlinear least squares fitting routine.

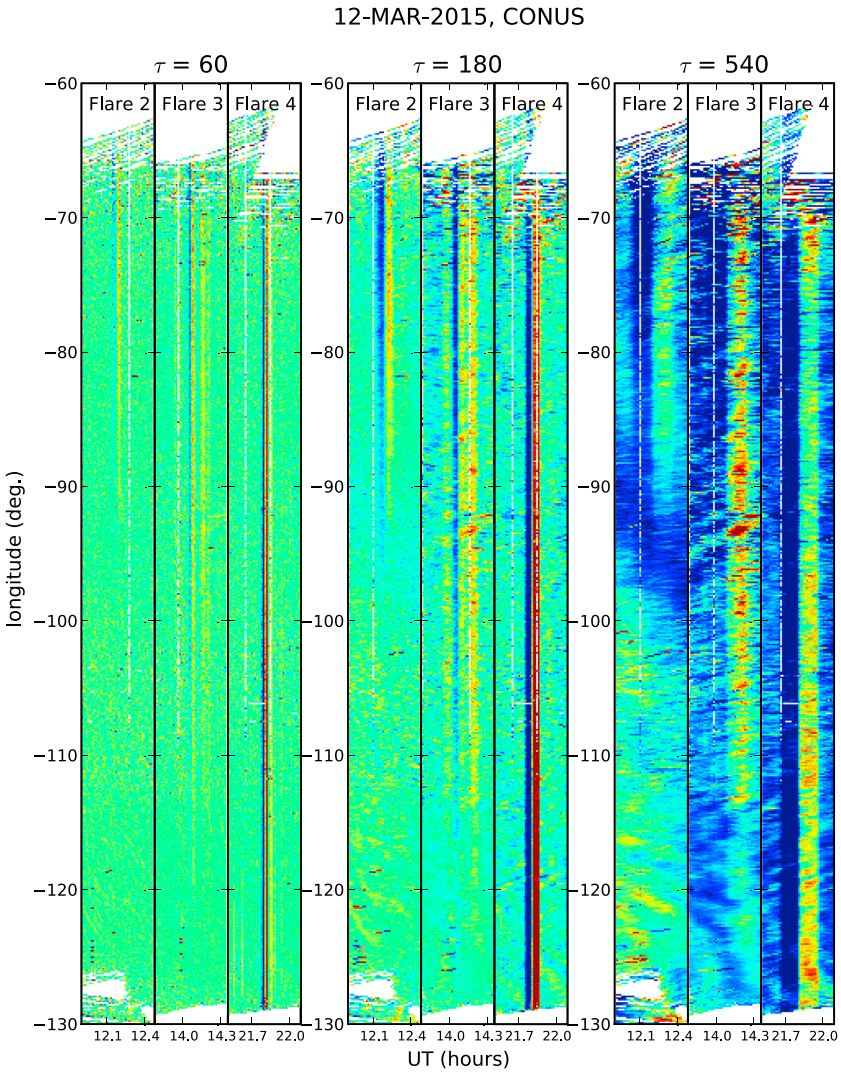

Figure 5. Zoomed-in images of mean relative TEC centered on the three M-class flares visible from CONUS. The color maps are identical to those used in Figure 3.

The detrended version of equation (1) fit to each flare and value of τ is plotted in Figure 7 in red. A curve computed using the average fitted parameters among all three τ's is shown per flare in blue; the "raw" version of this mean fitted function (i.e., not detrended) is shown in magenta in Figure 7 (bottom row). The best-fitting parameters for each flare are summarized within Table 2 with 1 σ uncertainties computed using the standard deviation among all three τ's.

A single step-function model per flare appears to reproduce well the observed pulses for all three τ's with the exception of Flare 3, which exhibits significantly more temporal structure than the rest. This is in sharp contrast to the X-ray morphology of Flare 3, which appears as a relatively well defined and narrow pulse. The TEC time series for the flare with the most X-ray temporal structure, Flare 2, is consistent with a single, somewhat gradual step function, further indicating that X-ray and TEC temporal morphology seem to be unrelated to some degree.

There also does not appear to be a significant correlation between TEC step strength and X-ray magnitude. For example, Flare 2 is by far the weakest in terms of X-rays, and yet its associated TEC increase is comparable to the others. However, there is some indication of a broader relationship between X-ray magnitude and TEC pulses since none of the data, either from CONUS or EU, show any signs of disturbances associated with the

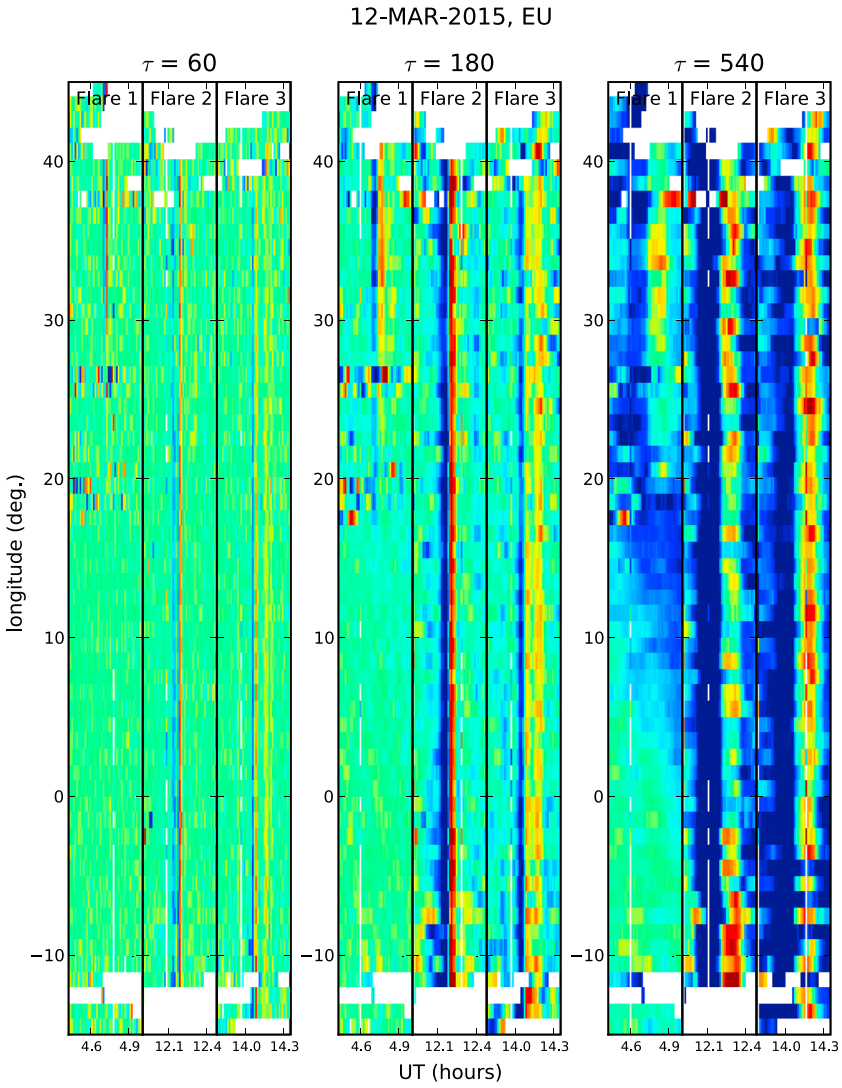

Figure 6. The same as Figure 5 but for EU.

several C-class flares implied by the GOES15 data (see Figure 1). We note that we have also looked within the SOHO-solar EUV monitor data archive for EUV data, which should be more directly related to TEC than X-ray irradiance. Unfortunately, no data were available for the four M-class flares presented here.

2.2. Small-Scale Impact

As indicated in section 1, two RF telescopes happened to be conducting separate and unique observations during the final flare of 12 March, aimed at characterizing ionospheric fluctuation for different purposes. The two observatories in question are colocated near 107.63°W, 34.07°N in western/central New Mexico. The first of these is the very large array (VLA), which was acquiring low-frequency (~350 MHz) observations of a bright radio galaxy via a new continuously operating backend, the VLA Low-band Ionosphere and Transient Experiment (VLITE). The second was the first station of the planned long wavelength array (LWA1), a dipole-based array that was observing ionospheric reflections of the HF radio station WWV at 10 MHz during the flare.

2.2.1. VLA and VLITE

The VLA is an interferometer consisting of 27 dish antennas, each 25 m in diameter. They are arranged in an inverted "Y" pattern that is periodically cycled among four configurations spanning 40, 11, 4, and 1 km each, referred to as A, B, C, and D, respectively. It is optimized for microwave observations through a Cassegrain system with the feeds in the middle of each dish. However, it has also been outfitted with a "P band" (~250–450 MHz) system, which uses crossed dipole feeds mounted at the Cassegrain systems' subreflectors. This unique feature allows, in principle, the P band signal to be captured and processed independently no

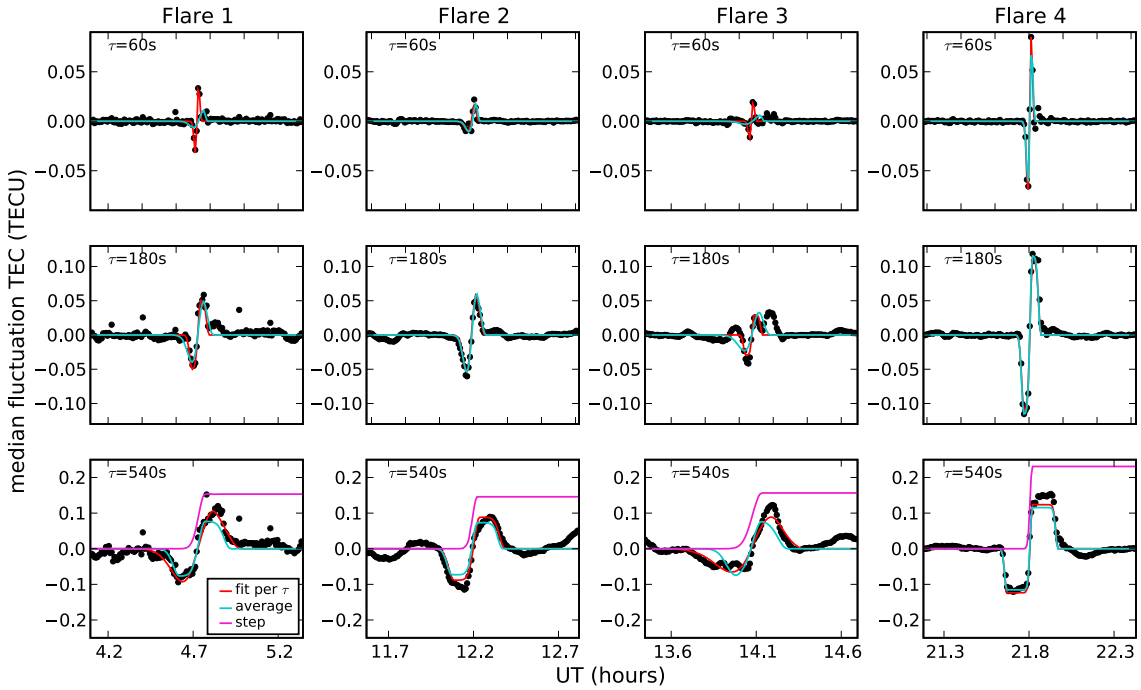

Figure 7. For each of the four flares, the median fluctuation TEC as a function of time for different values of the detrending parameter τ. Within each panel, the result of fitting a (detrended) smoothed step function given by equation (1) to each time series is plotted in red; the average fit over all τ's is plotted in blue. The actual smoothed step function is plotted within each panel in Figure 7 (bottom row) in magenta.

matter what higher-frequency feed is being used by the primary observer. This concept has been put into practice on 10 VLA antennas through the VLITE program.

Officially beginning its nominal 3 year lifetime in November 2014, VLITE continuously acquires and processes a portion of the P band passband (320–384 MHz) during all normal VLA operations. The data are processed with separate hardware and computing systems to yield low-frequency images of the sky wherever the VLA "looks." However, it is impossible to achieve high-fidelity imaging at these frequencies without accounting for distortions caused by ionospheric fluctuations. Specifically, changes in the TEC horizontal gradient lead to phase differences among the antennas within the array that can cause individual sources to appear to move on the sky, or in the worst cases, to be blurred beyond recognition. Consequently, techniques have been developed over the past few decades to correct for the effects of these fluctuations, and they are applied within the VLITE imaging process.

While a nuisance to astronomers, the sensitivity of the VLA at low frequencies to relatively fine-scale fluctuations of the TEC gradient can be a useful asset for ionospheric and even plasmaspheric remote sensing. To this end, a series of recent papers has described in detail how VLA data below 500 MHz can be used to detect and characterize TEC gradient fluctuations with amplitudes as small as 0.0002 TECU km^{-1} [see *Helmboldt et al.*, 2012a, 2012b; *Helmboldt and Intema*, 2012, 2014]. This is chiefly done by determining the TEC gradient at each VLA antenna from observations of a relatively bright cosmic source. These TEC gradient time series are then combined with a specialized spectral analysis to yield a three-dimensional (one temporal, two spatial) fluctuation spectrum cube. Within these spectra, a wave-like disturbance will manifest as a point-like source,

Table 2. Flare TEC Properties

Flare No.	Amplitude (TECU)	Peak UT	Rise Time (Min)
1	0.15 ± 0.08	4.77 ± 0.04	2.3 ± 2.2
2	0.15 ± 0.02	12.22 ± 0.01	1.7 ± 0.2
3	0.16 ± 0.14	14.13 ± 0.07	3.4 ± 3.8
4	0.23 ± 0.01	21.82 ± 0.00	0.7 ± 0.1

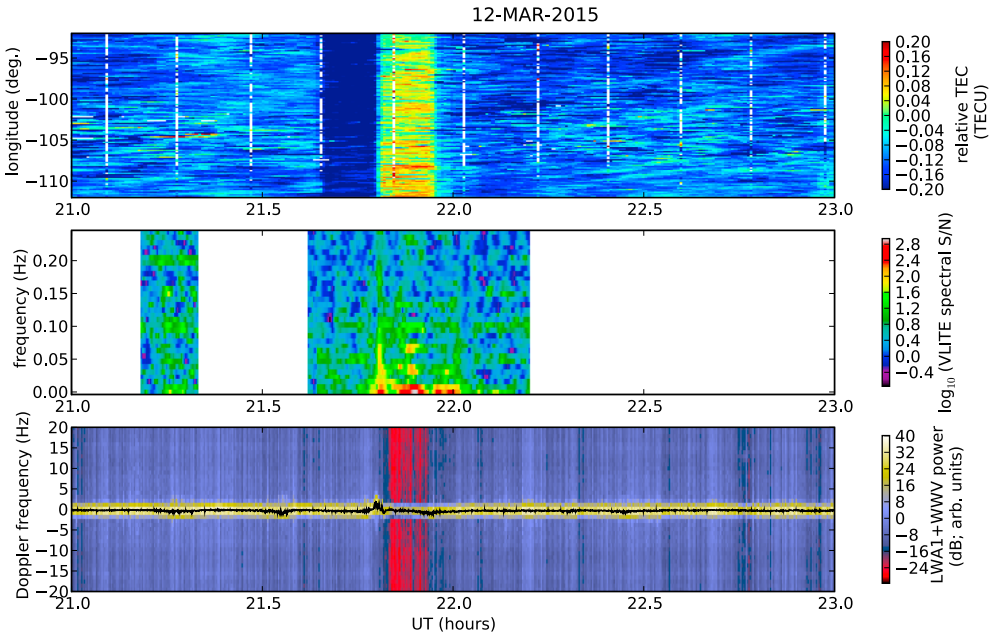

Figure 8. Near Flare 4: (top) the mean relative TEC in bins of time and longitude for longitudes near the two radio telescopes (the VLA and LWA1); (middle) the mean fluctuation spectrogram (normalized by the noise spectrum) of the TEC gradient from VLITE observations of 3C84; and (bottom) the spectrogram of the reflection of the WWV carrier signal as observed with LWA1.

the location of which gives its temporal and spatial frequencies, and subsequently, its horizontal velocity vector, $\vec{v}$. The extraction of TEC gradients (at 2 s intervals) and spectral analysis is performed on each VLITE "scan" (typically, 1–10 min of data) by an automated processing pipeline.

The VLA was observing and VLITE was acquiring data during the final two flares of 12 March while in the B configuration (spanning ∼11 km). Unfortunately, during Flare 3, the observed field contained only relatively faint low-frequency cosmic sources and the data were essentially unusable for ionospheric analysis. However, during Flare 4, a series of short 20 s scans of the bright radio galaxy 3C84 (or "Perseus A") were executed. Since these scans are too short to be processed automatically by the pipeline, they were concatenated into a single observation and then reprocessed.

Figure 8 (middle) shows a mean TEC gradient fluctuation spectrogram before and after Flare 4. A portion of the GPS TEC image ($\tau = 540$ s) spanning longitudes near the VLA is shown in Figure 8 (top) for comparison. The VLITE spectrogram is normalized by the corresponding noise spectrum, which is determined by processing the difference between the TEC gradients determined from the two linear polarization data streams (recall that the P band feeds are crossed dipoles). The fluctuation power abruptly changes near the X-ray and TEC peaks of the flare. This increase is brief and can be seen up to oscillation frequencies of about 0.08 Hz. Following this, an enhanced period of activity is apparent that is mostly confined to lower oscillation frequencies (∼0.01 Hz) and lasts a few minutes longer than the interval of TEC enhancement seen within the GPS data.

To explore the nature of the VLITE-detected fluctuations further, the three-dimensional spectral analysis described above was performed on the TEC gradient data every 1.5 min within 3 min windows. Only temporal frequencies >0 and <0.074 Hz were used to focus on the dominant fluctuations coincident with the flare (see Figure 8). We also only examined those disturbances with measured wavelengths >6 km. This discrimination was applied to avoid artifacts resulting from the impulse response of the 10-antenna, B-configuration VLITE system, which has strong sidelobes at spatial frequencies of (ξ_{EW}, ξ_{NS})=(0.22,-0.039) km^{-1} and (ξ_{EW}, ξ_{NS})=(−0.21, 0.035) km^{-1}.

Examination of the dominant fluctuations showed that they all appeared to be moving toward the southeast with wavelengths of 15–50 km. These characteristics are broadly consistent with a class of plasmaspheric irregularities discovered with the VLA by *Jacobson and Erickson* [1993]. Field-aligned irregularities (FAIs) formed within the plasmasphere will appear as roughly magnetic eastward directed wavefronts against the

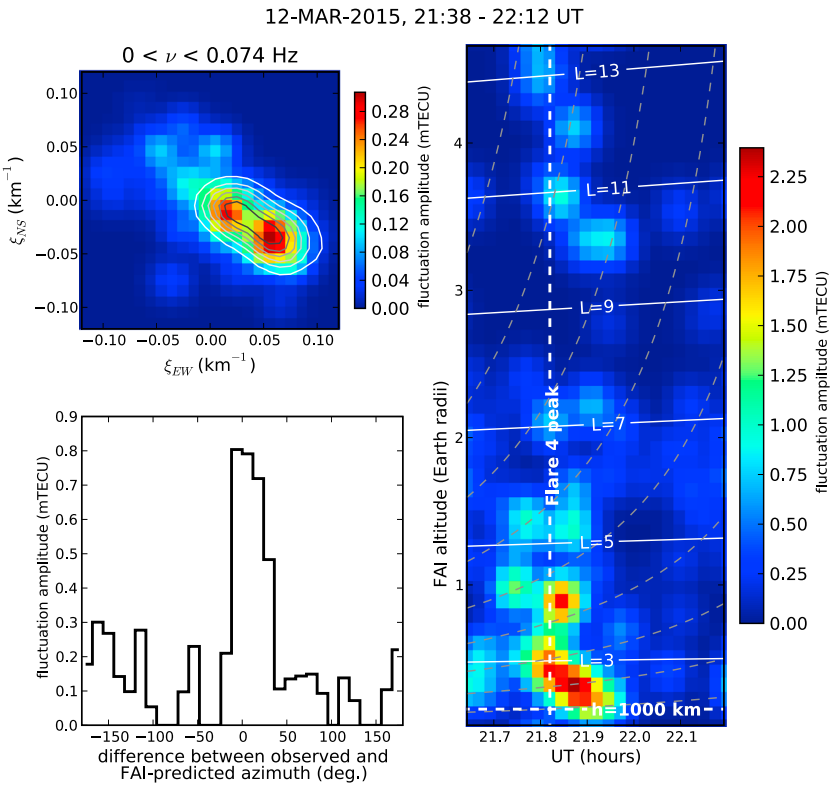

Figure 9. Analysis of VLITE observations of 3C84 before, during, and after Flare 4. (top left) The two-dimensional spatial frequency distribution of TEC gradient fluctuations for temporal frequencies <0.075 Hz. The grey-scale contours show the distribution if the measured azimuths are replaced with those calculated assuming corotating field-aligned irregularities (FAIs). (bottom left) The distribution of the difference between the observed fluctuation azimuths and those of corotating FAIs with the same speeds. (right) The inferred distribution of corotating FAI altitudes as a function of time. McIlwain *L* parameter values are plotted as white contours; grey contours show lines of constant geomagnetic longitude spaced by 2°.

cosmic background observed with the VLA due to the fact that the plasmasphere (nearly) corotates with the Earth. While such irregularities contribute very little to the local TEC, they can cause significant TEC gradients on scales of tens of kilometers that rival or even surpass in magnitude those resulting from ionospheric contributions [see *Jacobson and Erickson*, 1993; *Helmboldt and Intema*, 2012].

The expected apparent velocity vector for a plasmaspheric FAI depends on its location relative to both the telescope and the cosmic source. The apparent motion will be entirely perpendicular to the line of sight and will have a magnitude of $R\cos(\delta)\omega_e$, where R is the distance to the FAI, δ is the declination of the cosmic source (its angular distance above the celestial equator), and ω_e is the angular rotation rate of the Earth. Thus, the distance to a candidate plasmaspheric FAI can be computed according to its measured speed perpendicular to the line of sight. We note that the spectral analysis performed here on the VLITE data used antenna positions projected perpendicular to the line of sight (called *u* and *v* in radio astronomer parlance) for this purpose.

With a tentative distance computed, one may use the known orientation of the observed line of sight with a dipole model for the Earth's magnetic field to compute the apparent orientation of the magnetic field at the FAI's location within the u, v coordinate system. The expected azimuth of the velocity/wave number vector for the FAI will then be 90° east of this (for the Northern Hemisphere). A similar analysis method was used by *Hoogeveen and Jacobson* [1997] to establish that the magnetic eastward directed waves first seen with the VLA by *Jacobson and Erickson* [1992] were in fact located within the plasmasphere.

Figure 9 (top left) shows the two-dimensional (noise-corrected) distribution of spatial frequencies among all fluctuations detected with VLITE between 21:38 and 22:12 UT. As stated above, the strongest features are in the southeast quadrant with two peaks corresponding to wavelengths of about 15 and 50 km. These have measured speeds of roughly 100–150 m s^{-1} and 300–350 m s^{-1}, respectively. To establish whether or not

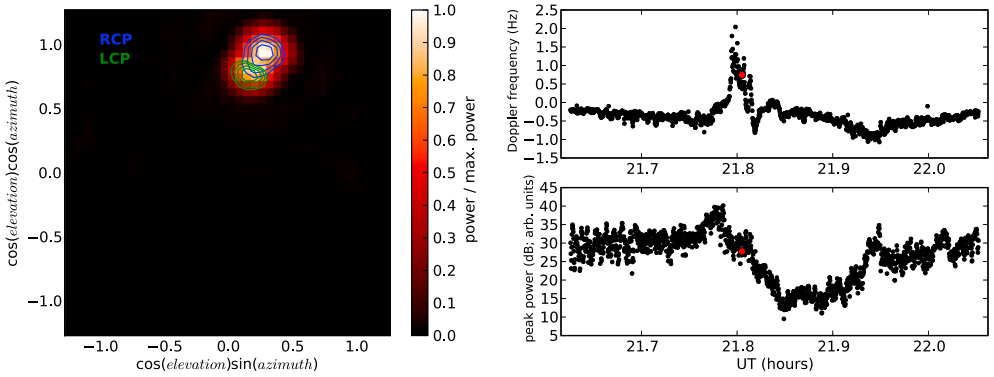

Figure 10. A frame from a movie showing the LWA1 data before, after, and during Flare 4. (left) The Stokes I all-sky image of the 10 MHz sky wave; contours of the right circular polarization (RCP) and left circular polarization (LCP) intensities are overlaid in blue and green, respectively. (right) The Doppler frequency and received power (Stokes I) of the carrier signal with red dots indicating the time step in Figure 10 (left).

these may be plasmaspheric FAIs, the expected azimuth was computed separately for each VLITE-detected irregularity using its measured speed and the orientation of the VLITE line of sight. The spatial frequency distribution was then recomputed, this time substituting the expected azimuths for the measured ones. This is plotted as grey-scale contours in Figure 9 (right) and nearly matches the two dominant features exactly.

A histogram of the difference between the expected and measured azimuths is also shown in Figure 9 (bottom). One can see that there is a slight systematic offset of a few degrees, which is likely due to the limitations of the assumed simple dipole magnetic field. However, it is clear that the strongest of the detected wave-like disturbances follow the expectations for plasmaspheric FAIs almost exactly.

It should be noted that southeastward directed TIDs are known to be prevented within the daytime in the Northern Hemisphere [e.g., *Hernández-Pajares et al.*, 2006; *Tsugawa et al.*, 2007b; *Hernández-Pajares et al.*, 2012b], which are thought to be caused by wind-filtered gravity waves [e.g., *Afraimovich et al.*, 1999]. As noted in section 2.1, there is evidence of such gravity waves within the GPS data near in time to Flare 4 with zonal speeds ∼100–150 m s^{-1}. However, they are not apparent within data near the VLA's longitude (see Figure 8 (top)) and have much larger wavelengths (∼100 km) than the VLITE-detected irregularities that had similar speeds. In addition, as we will show below, the slower VLITE-detected irregularities actually appear to slow down with time, whereas the GPS-detected TIDs appear to maintain the same phase speeds over roughly 1–2 h. This indicates that the dominant VLITE-detected fluctuations are due to plasmaspheric FAIs.

Adopting the assumption that the predominant TEC gradient fluctuations are plasmaspheric FAIs, we have computed the distribution of these as a function of time and altitude; the result of which is shown in Figure 9 (right). Lines of constant McIlwain *L* parameter are plotted in white; lines of constant geomagnetic longitude are plotted in grey. One can see the two populations of irregularities that formed near the peak of the flare. There is some evidence that the higher/faster FAIs formed before the peak of the flare at a height of about 5600 km ($L \simeq 4.0$). About 1–2 min after the flare peak, they increase in strength, then quickly disappear. The slower/lower FAIs first appear right at the flare peak at an altitude of about 2600 km ($L \simeq 2.8$), then seem to slow down/descend steadily over a period of ∼7 min to an altitude of 1450 km ($L \simeq 2.4$), then likewise disappear.

2.2.2. LWA1 and WWV

LWA1 is the first of roughly 50 individual "stations" of phased arrays intended to be distributed throughout New Mexico and used as a large interferometric telescope. LWA1 consists of 256 bent dipole antennas in a pseudo-random configuration spanning roughly 100 m. The antennas are sky noise limited over the entire 20–80 MHz range and can be operated from 10–88 MHz. LWA1 is currently run as a stand-alone observatory, offering both a phase array/beamforming mode, and an "all-sky" mode that records the output from each antenna to be combined after the fact to form all-sky images. For more details, see *Hicks et al.* [2012]; *Taylor et al.* [2012]; *Ellingson et al.* [2013].

Helmboldt et al. [2013] showed that LWA1 can be used to detect and monitor ionospheric reflections or "sky waves" from the National Institute of Standards and Technology HF radio station WWV near Ft. Collins, Colorado. WWV broadcasts coded signals that convey the current time at 2.5, 5, 10, 15, and 20 MHz.

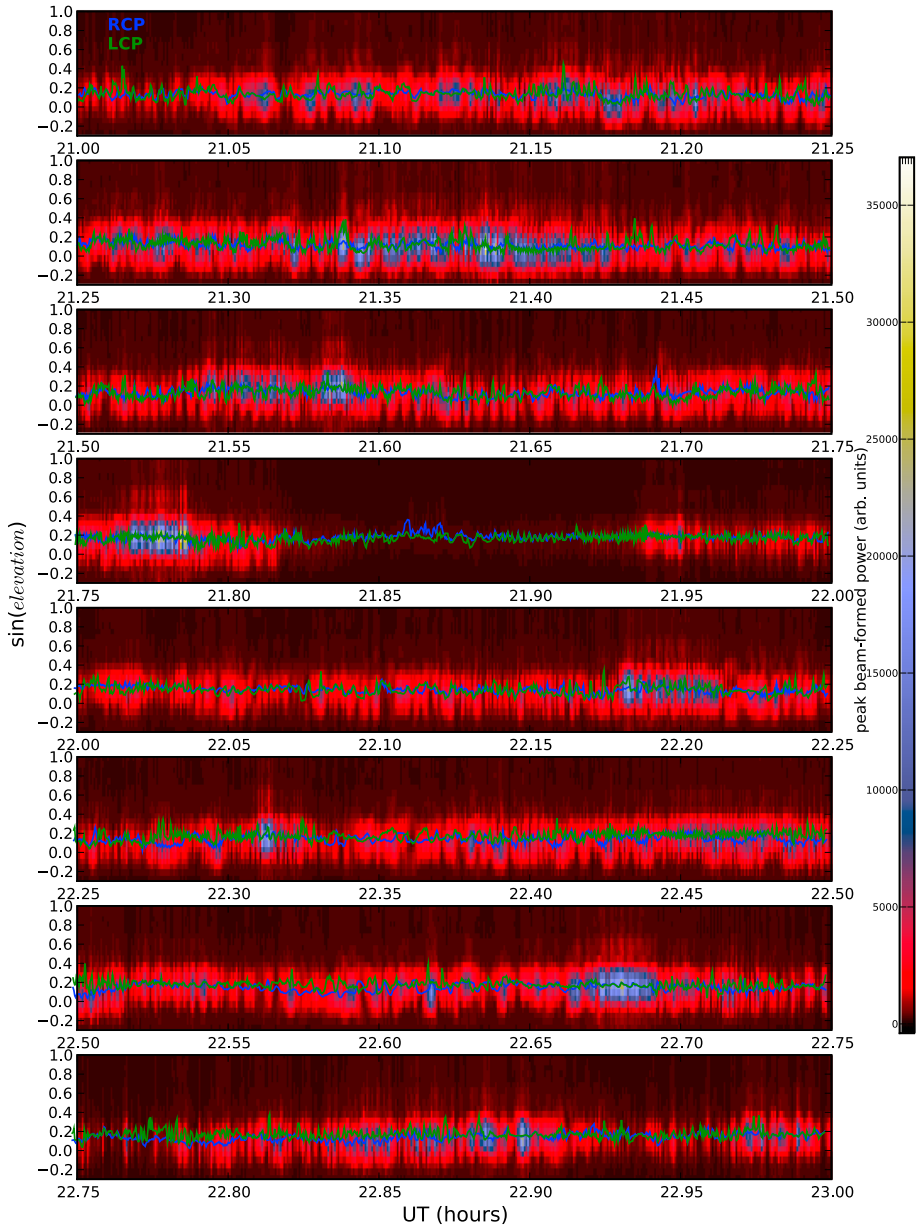

Figure 11. The received power (Stokes I) of the WWV 10 MHz carrier signal as a function of time (abscissa) and elevation (ordinate). The peak elevation as a function time is also plotted for the RCP and LCP sky waves in blue and green, respectively.

The WWV signal includes a 5 ms pulse at the beginning of each UT second that can be used for ranging and a carrier signal that can be used to monitor small time scale Doppler fluctuations (see *Nelson et al.*, 2005, for a more complete discussion of the WWV signal). The 10 MHz WWV sky wave is nearly always visible to LWA1; 15 and 20 MHz signals are detected under certain circumstances (e.g., when sporadic *E* is present). The signal processing methods used to perform all-sky passive radar and Doppler monitoring with LWA1 and WWV are detailed within *Helmboldt et al.* [2013].

LWA1 was observing on 12 March from 21:00–23:00 UT in its all-sky mode at 10 MHz as part of a separate program to use the WWV sky wave to monitor the ionosphere in the aftermath of surface explosions. By pure happenstance, the impact of a different kind of explosion was detected, the final M-class solar flare of that day. This is shown in Figure 8 (bottom) (with GPS and VLITE data for comparison) where we display the spectrogram (Stokes I power) of the WWV carrier signal at time and frequency resolutions of 1.024 s and 0.098 Hz,

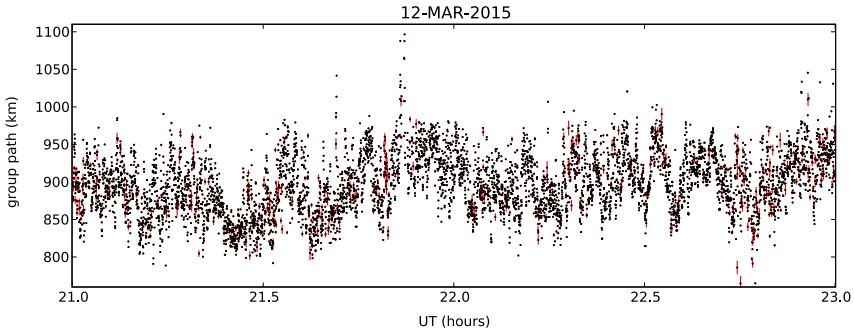

Figure 12. The group path (Stokes I) as a function of time derived from the modulated on-the-second pulse within the WWV 10 MHz signal. 1 σ error bars are shown in red but only for those points where the plotting symbols are larger than the errors.

averaged over all LWA1 antennas. Near the X-ray peak of the flare, when the period of TEC enhancement commences within the GPS data, there is a noticeable and brief disturbance in the Doppler frequency, followed by an sudden drop in received power. The power loss is presumably the result of absorption due to increased ionization within the *D* region and lasted ~10 min. This is a well-known feature of SIDs, and the duration of this absorption event is roughly consistent with past observations [see, e.g., *Appleton and Piggott*, 1954].

Both the Doppler frequency and received power time series are shown in more detail in Figure 10 (right). Figure 10 (left) shows an all-sky, Stokes I image of the WWV carrier signal for the time highlighted with red dots in Figure 10 (right). Because the ionospheric index of refraction at any given location is different for right and left circular polarization (RCP and LCP, respectively), the paths those components of the WWV signal take to LWA1 may not be the same. Therefore, RCP and LCP images were also generated via appropriate combinations of the beamformed complex voltages for the *X* and *Y* linear polarization feeds. We note that only the standard LWA1 instrumental calibration [*Dowell et al.*, 2012] was applied to these data during the beamforming process and that there is likely some polarization "leakage" due to differences in the effective antenna patters for the two feeds per antenna. The contours for the estimated RCP and LCP sky waves are overlaid on the image in Figure 10 (left) in blue and green, respectively.

The time step displayed in Figure 10 is essentially in the middle of the Doppler disturbances and shows a double-peaked sky wave. From the contours, one can see that this is the result of the RCP and LCP signal components traveling along significantly different paths due to the disturbed state of the ionosphere. This figure is one frame of a Movie S1 in the supporting information showing all-sky images over the entire time range plotted in Figure 10 (right). From these, one can see significant movement of the sky wave, especially during the disturbed period after the flare, including several instances of double-peak sky waves. We illustrate this further in Figure 11, which shows the peak power as a function of sin(elevation) in the direction of WWV. This was done by rotating each all-sky image anticlockwise by 16.5°, the angle between due north and the great circle between LWA1 to WWV. We then measured the peak power along the ordinate within the top half of each rotated image and reversed the order of the result. These were concatenated into a time series to make the images shown in Figure 11. We have also plotted within these panels the peak elevations of the RCP and LCP sky waves as functions of time in blue and green, respectively. One can see two instances during the disturbed period of reduced received power where the signal elevation jumped significantly within the span of 1–2 s, especially for the RCP component. This would lead to significantly different paths within a single coherent integration for the typical over-the-horizon (OTH) radar system, which uses integration lengths of ~10 s [e.g., *Headrick and Thomason*, 1998; *Nickisch et al.*, 2012]. This effect would be compounded by the fact that typical operational OTH radars use monopole receiving antennas and therefore have no means by which to separate the two circular polarization components.

As described above, the 5 ms pulse emitted by WWV every second allows for ranging of the reflected signal. The pulse processing described by *Helmboldt et al.* [2013] was applied to the 12 March observations, and the resulting group path time series is shown in Figure 12. The typical group path was about 900–950 km, implying a virtual reflection height of 230–280 km. The flare seems to have had very little impact on the group path, except for a brief (~1 min) jump from about 990 to 1050 km shortly after the X-ray peak of the flare. We note that the typical signal-to-noise ratio of the detected pulse is about 8100; given the processed pulse

width of 10 ms, this implies a group path precision of <1 km (see the error bars in Figure 12). Thus, this rapid 60 km jump in group path appears to be a significant deviation. We also note that when the radar analysis was performed separately using RCP and LCP complex voltages, the nature of the temporal behavior of the group paths for both appeared similar with the same 60 km jump near the flare peak apparent for both.

3. Summary and Discussion

Our investigation into the ionospheric response to a series of M-class solar flares has revealed several interesting features. Through analysis of data from thousands of GPS receiver stations, we found that each of the four flares induced a hemispheric step increase in TEC, each with an amplitude of roughly 0.2 TECU. The GPS data also demonstrated that when TIDs were present, the flare-induced step increase enhanced their appearance as well.

The magnitudes of the TEC step increases do not appear well correlated with peak X-ray intensity. However, the X-ray peaks are all roughly the same order of magnitude, and the correlation between flare X-ray intensity and TEC rate of increase found by *Hernández-Pajares et al.* [2012a] shows a significant amount of inherent scatter for relatively X-ray faint flares. Thus, the small number statistics involved here make it difficult to draw any meaningful conclusions from the lack of correlation, other than it is consistent with the amount of scatter within the *Hernández-Pajares et al.* [2012a] relation.

Observations with the VLITE system on the VLA showed evidence of plasmaspheric disturbances that commenced at the time of the X-ray peak for Flare 4. These appear within two main groups. The first appeared at a relatively high L shell (∼4) and did not last long (1–2 min). The second appeared lower ($L \simeq 2.4$–2.8) and for longer, about 7 min. The second group of plasmaspheric irregularities seemed to descend over time, but this is likely something of an illusion, resulting from the geometry of the observations. If one examines Figure 9 (right), one will see that the elongated morphology of this group of disturbances in height and time runs roughly perpendicular to lines of constant geomagnetic longitude. Given this, it seems likely that these lie within a disturbed region of the plasmasphere between L shells of 2.4 and 2.8 that is roughly 2° wide in longitude. The apparent drop in height with time can then be explained by the movement of the line of sight through this region and the geometry of both the observations and the disturbed flux tube(s).

From the available data, it is not clear why this region and the smaller disturbed region seen near $L \simeq 4$ stand out. An examination of the available GPS data at the same time and within the same range of geomagnetic longitudes showed that the regions to which the disturbed L shells map do not appear more disturbed than the surrounding regions in terms of TEC. Thus, unusually large variations in ion pressure at ionospheric altitudes can likely be ruled out as the source. It may be that these plasmaspheric regions were more disturbed to begin with and that an increased influx of ions following the flare simply made the irregularities more "visible" to VLITE. Indeed, there is some evidence of relatively weak disturbances near $L \simeq 4$ preceding the peak of the flare (see Figure 9). Regardless of the exact origin of the disturbances themselves, the fact that they appear near the peak of the flare lends credence to the scenario proffered by *Leonovich and Tashchilin* [2008]. They calculated that the topside ionosphere is temporality evacuated at flare onset due to an increase in ion pressure within the *F* region and the rate of flow of material up flux tubes to the plasmasphere.

LWA1 observations at 10 MHz of ionospheric reflections of the HF radio station WWV indicated that the X-ray peak of the flare is associated with an *F* region (∼250 km altitude) disturbance, manifested as relatively large Doppler frequency fluctuations (amplitude ∼2 Hz or 60 m s^{-1}) lasting a few minutes. The fact that this coincides with the appearance disturbed plasmaspheric regions may indicate that this *F* region disturbance is related to a sudden increase in ion outflow to the plasmasphere. The LWA1 data also show that the bulk of the postflare period of TEC enhancement is associated with increased *D* region absorption. This implies, as expected, that the increase in ion production due to the flare extends down to the very bottom of the ionosphere.

Whether the results presented here are typical for M-class flares or are unique to the series of 12 March 2015 flares remains to be seen. With the continuous operation of VLITE and a complementary GPS-based analysis pipeline being run daily on data from New Mexico-based GPS receivers, a larger, statistical analysis of both ionospheric and plasmaspheric irregularities associated with flares will be possible. The analysis presented here will serve as a framework that may inform and guide this larger survey moving forward.

We also note that our results contain implications about the impact of even moderate-strength flares on operational systems. Specifically, the LWA1 observations of WWV indicate that a spread in observed Doppler frequency at 10 MHz within a typical coherent integration time will be as high as 1.5 Hz, the equivalent of 45 m s^{-1} or 162 kph in Doppler speed. This makes it difficult to use these systems to distinguish between clutter and targets. While the Doppler disturbance associated with Flare 4 only lasted a few minutes, a closely spaced series of such flares could be extremely detrimental to OTH radar capabilities. In addition, as mentioned in section 2.2.2, the longer period of lowered HF power associated with Flare 4 appeared more susceptible to largely divergent paths for the RCP and LCP signal components. This is something that is also highly problematic for OTH radar systems using monopole receiving antennas.

Acknowledgments
The authors would like to thank the reviewers as well as S. White and S. Tun for their useful comments and suggestions. Data supporting this paper are available upon request submitted via email to the author at joe.helmboldt@nrl.navy.mil. Basic research at the Naval Research Laboratory is supported by 6.1 base funding. The National Radio Astronomy Observatory is a facility of the National Science Foundation operated under cooperative agreement by Associated Universities, Inc. The authors are grateful to MIT Haystack Observatory for the GPS TEC data obtained from their Madrigal data center. Construction of the LWA has been supported by the Office of Naval Research under contract N00014-07-C-0147. Support for operations and continuing development of the LWA1 is provided by the National Science Foundation under grant AST-1139974 of the University Radio Observatory program.

References

Afraimovich, E. L., O. N. Boitman, E. I. Zhovty, A. D. Kalikhman, and T. G. Pirog (1999), Dynamics and anisotropy of traveling ionospheric disturbances as deduced from transionospheric sounding data, *Radio Sci.*, *34*, 477–487, doi:10.1029/1998RS900004.

Afraimovich, E. L., E. A. Kosogorov, and L. A. Leonovich (2000), The use of the international GPS network as the global detector (GLOBDET) simultaneously observing sudden ionospheric disturbances, *Earth Planets Space*, *52*, 1077–1082, doi:10.1186/BF03352334.

Appleton, E. V., and W. R. Piggott (1954), Ionospheric absorption measurements during a sunspot cycle, *J. Atmos. Terr. Phys.*, *5*, 141–172, doi:10.1016/0021-9169(54)90029-X.

Atac, T. (1991), On the SID durations, *Astrophys. Space Sci.*, *181*, 157–159, doi:10.1007/BF00644123.

Dmitriev, A. V., and H.-C. Yeh (2008), Geomagnetic signatures of sudden ionospheric disturbances during extreme solar radiation events, *J. Atmos. Sol. Terr. Phys.*, *70*, 1971–1984, doi:10.1016/j.jastp.2008.05.008.

Dodson, H. W., and E. R. Hedeman (1958), Crochet-associated flares, *Astrophys. J.*, *128*, 636, doi:10.1086/146577.

Dowell, J., D. Wood, K. Stovall, P. S. Ray, T. Clarke, and G. Taylor (2012), The long wavelength array software library, *J. Astron. Instrum.*, *1*, 1250006, doi:10.1142/S2251171712500067.

Ellingson, S. W., et al. (2013), The LWA1 radio telescope, *IEEE Trans. Antennas Propag.*, *61*, 2540–2549, doi:10.1109/TAP.2013.2242826.

Ellison, M. A. (1950), Ionospheric effects of solar flares, *Mon. Not. R. Astron. Soc.*, *110*, 626.

Field, E. C. (1970), VLF and ELF propagation during sudden ionospheric disturbances, *J. Geophys. Res.*, *75*, 1927–1933, doi:10.1029/JA075i010p01927.

Headrick, J. M., and J. F. Thomason (1998), Applications of high-frequency radar, *Radio Sci.*, *33*, 1045–1054, doi:10.1029/98RS01013.

Helmboldt, J. F., and H. T. Intema (2012), Very large array observations of disturbed ion flow from the plasmasphere to the nighttime ionosphere, *Radio Sci.*, *47*, RS0K03, doi:10.1029/2012RS004979.

Helmboldt, J. F., and H. T. Intema (2014), Advanced spectral analysis of ionospheric waves observed with sparse arrays, *J. Geophys. Res. Space Physics*, *119*, 1392–1413, doi:10.1002/2013JA019162.

Helmboldt, J. F., T. J. W. Lazio, H. T. Intema, and K. F. Dymond (2012a), High-precision measurements of ionospheric TEC gradients with the Very Large Array VHF system, *Radio Sci.*, *47*, RS0K02, doi:10.1029/2011RS004883.

Helmboldt, J. F., T. J. W. Lazio, H. T. Intema, and K. F. Dymond (2012b), A new technique for spectral analysis of ionospheric TEC fluctuations observed with the Very Large Array VHF system: From QP echoes to MSTIDs, *Radio Sci.*, *47*, RS0L02, doi:10.1029/2011RS004787.

Helmboldt, J. F., et al. (2013), Passive all-sky imaging radar in the HF regime with WWV and the first station of the Long Wavelength Array, *Radio Sci.*, *48*, 491–512, doi:10.1002/rds.20056.

Hernández-Pajares, M., J. M. Juan, and J. Sanz (2006), Medium-scale traveling ionospheric disturbances affecting GPS measurements: Spatial and temporal analysis, *J. Geophys. Res.*, *111*, A07S11, doi:10.1029/2005JA011474.

Hernández-Pajares, M., A. GarcíA-Rigo, J. M. Juan, J. Sanz, E. Monte, and A. Aragón-ÀNgel (2012a), GNSS measurement of EUV photons flux rate during strong and mid solar flares, *Space Weather*, *10*, S12001, doi:10.1002/2012SW000826.

Hernández-Pajares, M., J. M. Juan, J. Sanz, and A. Aragón-ÀNgel (2012b), Propagation of medium scale traveling ionospheric disturbances at different latitudes and solar cycle conditions, *Radio Sci.*, *47*, RS0K05, doi:10.1029/2011RS004951.

Hicks, B. C., et al. (2012), A wide-band, active antenna system for long wavelength radio astronomy, *Publ. Astron. Soc. Pac.*, *124*, 1090–1104, doi:10.1086/668121.

Hoogeveen, G. W., and A. R. Jacobson (1997), Improved analysis of plasmasphere motion using the VLA radio interferometer, *Ann. Geophys.*, *15*, 236–245, doi:10.1007/s00585-997-0236-6.

Jacobson, A. R., and W. C. Erickson (1992), Wavenumber-resolved observations of ionospheric waves using the Very Large Array radiotelescope, *Planet. Space Sci.*, *40*, 447–455, doi:10.1016/0032-0633(92)90163-I.

Jacobson, A. R., and W. C. Erickson (1993), Observations of electron density irregularities in the plasmasphere using the VLA radio interferometer, *Ann. Geophys.*, *11*, 869–888.

Kaufmann, P., L. Rizzo Piazza, J. H. Fernandez, and M. Rocha da Silva (2002), Solar flares not producing sudden phase advances, *J. Geophys. Res.*, *107*(A8), 1219, doi:10.1029/2001JA000292.

Leonovich, L. A., and A. V. Tashchilin (2008), Disturbances in the topside ionosphere during solar flares, *Geomag. Aeron.*, *48*, 759–767, doi:10.1134/S001679320806008X.

Liu, J. Y., C. H. Lin, H. F. Tsai, and Y. A. Liou (2004), Ionospheric solar flare effects monitored by the ground-based GPS receivers: Theory and observation, *J. Geophys. Res.*, *109*, A01307, doi:10.1029/2003JA009931.

Matsushita, S. (1976), Ionospheric and thermospheric responses during August 1972 storms—A review, *Space Sci. Rev.*, *19*, 713–737, doi:10.1007/BF00210648.

Munton, D. C., B. W. Tolman, R. B. Harris, A. J. Kerkhoff, T. L. Gaussiran, G. S. Bust, and S. L. Nelsen (2004), GPSTk: An open source toolkit for working with GPS data, *AGU Fall Meeting Abstracts*, p. A123.

Nelson, G. K., M. A. Lombardi, and D. T. Okayama (2005), NIST time and frequency radio stations: WWV, WWVH, and WWVB, *NIST Special Publication, 250-67*.

Nickisch, L. J., G. St. John, S. V. Fridman, M. A. Hausman, and C. J. Coleman (2012), HiCIRF: A high-fidelity HF channel simulation, *Radio Sci.*, *47*, RS0L11, doi:10.1029/2011RS004928.

Pacini, A. A., and J.-P. Raulin (2006), Solar X-ray flares and ionospheric sudden phase anomalies relationship: A solar cycle phase dependence, *J. Geophys. Res.*, *111*, A09301, doi:10.1029/2006JA011613.

Qian, L., A. G. Burns, S. C. Solomon, and P. C. Chamberlin (2012), Solar flare impacts on ionospheric electrodyamics, *Geophys. Res. Lett.*, *39*, L06101, doi:10.1029/2012GL051102.

Taylor, G. B., et al. (2012), First light for the first station of the Long Wavelength Array, *J. Astron. Instrum.*, *1*, 1250004, doi:10.1142/S2251171712500043.

Tsugawa, T., S.-R. Zhang, A. J. Coster, Y. Otsuka, J. Sato, A. Saito, Y. Zhang, and L. J. Paxton (2007a), Summer-winter hemispheric asymmetry of the sudden increase in ionospheric total electron content and of the O/N_2 ratio: Solar activity dependence, *J. Geophys. Res.*, *112*, A08301, doi:10.1029/2007JA012415.

Tsugawa, T., Y. Otsuka, A. J. Coster, and A. Saito (2007b), Medium-scale traveling ionospheric disturbances detected with dense and wide TEC maps over North America, *Geophys. Res. Lett.*, *34*, L22101, doi:10.1029/2007GL031663.

Vazherkin, V. A., B. Laso, L. A. Lobachevskii, V. D. Novikov, and I. N. Odintsova (1980), Doppler study of ionospheric effects of solar flares, *Geomag. Aeron.*, *20*, 1009–1013.